An *LCC–LCC* Compensated WPT System With Switch-Controlled Capacitor for Improving Efficiency at Wide Output Voltages

Na Fu, Junjun Deng, *Member, IEEE*, Zhenpo Wang, *Senior Member, IEEE*, and Deliang Chen

***Abstract*—In this article, a triple-phase-shift (TPS) control strategy combining a switch-controlled capacitor (SCC) is proposed for *LCC–LCC* compensated wireless power transfer (WPT) system to improve the overall efficiency at wide output voltages. The basic mathematical model of the system is first established, and the conditions for zero-voltage switching (ZVS) and load matching are described under TPS. Then, the mechanism of TPS reducing system efficiency at wide output voltages is revealed based on the established model. An SCC is employed to adjust the compensation capacitance to achieve a minimum circulating reactive power on both sides and reduce the rectifier input current. Finally, the impact of the compensation capacitance variations on the current, output power, and impedance are analyzed, based on which the optimal value of adjustable capacitance for maximum efficiency is derived by further considering the established time domain model. A comparative experiment is performed with traditional TPS and the proposed control technique, which shows that the system with the proposed control technique achieves a higher efficiency over the TPS within the entire power range.**

***Index Terms*—Electric vehicles (EVs), *LCC–LCC* compensation, switch-controlled capacitor (SCC), wireless power transfer (WPT).**

I. Introduction

WIRELESS power transfer (WPT) technology has received increasing attention due to its safety, reliability, and convenience [1], [2]. Without plugging any charging cables, WPT provides an ideal solution for the automatic charging of electric vehicles (EVs) [3], [4]. Different EVs may have different internal battery voltages, which requires the WPT system to efficiently deliver the required charging power at different output voltages. In addition, the battery voltage varies dramatically with the state of charge. These two factors bring a great challenge for power regulation of the WPT system, especially in battery charging applications where constant voltage or current needs to be generated [5], [6].

To realize wide output power regulation for WPT system, numerous approaches have been proposed, which can be roughly categorized into two groups, i.e., with auxiliary dc–dc converters and with active rectification.

Adding auxiliary dc–dc converters on primary side, secondary side or both sides is an effective way to implement output regulation and maximum efficiency tracking [7], [8], [9]. However, such two-stage structure notably increases the overall volume and mass and degrades the system efficiency due to larger power losses. It is not the preferred choice considering the limited space, system efficiency, and cost.

To eliminate the cascaded dc–dc converter while preserving the overall controllability, an active rectifier at secondary side is an alternative choice to realize wide output modulation [10], [11]. It has been proven in [12] that the equivalent reactance of the active rectifier should be adjusted to its appropriate value for optimal efficiency. In this regard, Huang et al. [13] proposed a dual control strategy to achieve constant voltage output and load impedance matching. This strategy combined the operating frequency of the primary inverter and the phase angle of the secondary active rectifier. Unfortunately, regulation of the operating frequency over a wide range not only causes serious system detuning, thus significantly reducing the efficiency, but also leads to the bifurcation phenomenon [14]. To avoid regulating the frequency, dual-phase-shift (DPS) control method is proposed in [15]. The DPS method utilizes the phase angles of the primary inverter and the secondary active rectifier to track the optimal impedance [16], [17], [18], [19]. The main problem with the DPS method is the loss of zero-voltage switching (ZVS) operation, which increases the switching losses in the converter and dramatically decreases system efficiency. To address this issue, the triple-phase-shift (TPS) control scheme is proposed by introducing a third phase shift angle, i.e., using an outer phase shift between the inverter and rectifier [20]. In this method, two critical third phase shift angles were derived separately under ZVS conditions for the primary and secondary side, and the minimum of these two critical values is utilized to implement the third phase angle. Then, the ZVS of both sides is guaranteed.

Previous studies have described various methods for ensuring the ZVS operation and achieving impedance matching. However, challenges remain in how to further minimize the reactive

Manuscript received 10 June 2022; revised 24 November 2022 and 3 February 2023; accepted 13 March 2023. Date of publication 22 March 2023; date of current version 19 May 2023. This work was supported in part by the National Key Research and Development Program of China under Grant 2021YFB2501604, and in part by the National Natural Science Foundation of China under Grant 52177207. Recommended for publication by Associate Editor G. Grandi. *(Corresponding author: Junjun Deng.)*

The authors are with the Beijing Institute of Technology, Beijing 100081, China (e-mail: funa@bit.edu.cn; dengjunjun@bit.edu.cn; wangzhenpo@bit.edu.cn; chendeliang@bit.edu.cn).

Color versions of one or more figures in this article are available at https://doi.org/10.1109/TPEL.2023.3260207.

Digital Object Identifier 10.1109/TPEL.2023.3260207

power on both sides for a wide range of output voltage while effectively reducing the conduction and turn-off losses caused by high current stress on the receiver. Individually using the mentioned modulation methods, such as DPS or TPS, etc., cannot address these issues due to the limited control freedom.

The *LCC–LCC* compensation topology can provide more design freedom, so it is a promising topology to solve the aforementioned challenges without affecting the output power via a reasonable adjustment of compensation parameters [21], [22].

In this article, a switch-controlled capacitor (SCC) is added to the *LCC–LCC* compensated WPT system. The compensation capacitor value is adjusted by controlling the control angle of the SCC. This operation can achieve a high-power factor and reduce current stress at wide voltage outputs. The SCC technology was first proposed in [23] and it has been applied in various types of resonant converters [24], including the WPT systems [25], [26]. SCC used in WPT systems can compensate for inductance fluctuations caused by coil misalignment [27], [28], [29], or implement ZVS [30], [31]. To improve power output and system efficiency under coil misalignment, numerous approaches have been proposed based on the variable capacitor [32], [33]. The variable capacitor used in WPT systems can compensate for inductance fluctuations caused by coil misalignment [27], [28], [34], [35]. In terms of ZVS realization, Wang et al. [30] employed a hybrid control method of single-phase-shift and SCC for *LCC*-S topology to obtain wide output voltage regulation with ZVS. Nevertheless, the wide-range ZVS operation is achieved at the cost of increasing resonant current, which decreases system efficiency. Similar problems exist in the combined dual phase DPS and SCC control strategy. In [36], through adopting the SCC, *LCC–LCC* compensated WPT system implements ZVS of CV output procedure. However, only a single CV output can be implemented over the wide range load.

In contrast, this article proposed a TPS control strategy combining an SCC for *LCC–LCC* compensation topology to improve system efficiency. In the TPS control method, power and efficiency calculation models are first established, and the ZVS and load matching conditions are given. Based on these conditions, the relationship between two inner- and one outer-phase shift angles is established. Then, by analyzing the reactive power of the primary and secondary sides at wide output voltages, an SCC is added to the secondary side to adjust the series compensation capacitance. This can ensure a minimum circulating reactive power on both sides and reduce the input current of the rectifier. Finally, the impact of the compensation capacitance variations on the current, output power, and impedance are analyzed respectively, and the optimal value of adjustable capacitance can be derived based on the established time-domain model.

The main contributions of this manuscript are summarized as follows.

1) The relationship between the series compensation capacitance value of *LCC–LCC* topology and system output characteristics is established, and a calculation model of series compensation capacitance value is proposed for current stress reduction.

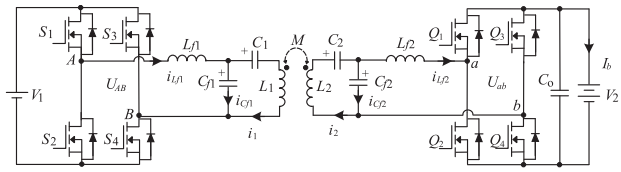

Fig. 1. *LCC–LCC* compensated WPT system with an active rectifier.

2) An optimal method of the series compensation capacitor value is put forward with the harmonic-considered time-domain model, which can be used to achieve ZVS operation with minimum reactive power as well as current stress reduction.
3) A control strategy combining SCC and TPS is proposed for CC or CV output with variable loads, which maximizes the system efficiency under wide voltage output conditions. An additional complicated control technique is not required in the proposed control strategy since SCC control loop is decoupled from the CC/CV control loop.

The rest of this paper is organized as follows. Section II presents the basic mathematical model and the conditions for ZVS and load matching under TPS. Section III introduces the proposed control strategy of SCC in conjunction with TPS for the LCC-LCC system. Section IV presents the diagram of the proposed control strategy. In Section V, a comparative experiment is conducted to demonstrate advantages of the proposed method. Finally, Section VI concludes this article.

II. Problem Formulation

A. System Structure

A typical *LCC–LCC* compensated WPT system with an active rectifier is shown in Fig. 1, which consists of two H-bridge converters and the *LCC* compensation circuit. V_1 and V_2 represent the dc power source and the battery voltage respectively. M is the mutual inductance and the coupling coefficient k is defined as $k = M/\sqrt{L_1 L_2}$. For easy description, in Fig. 1, the power source side is defined as the primary side, and the EV side is defined as the secondary side.

Fig. 2 shows the main waveforms of the WPT system under TPS control. β_p is the phase angle of U_{AB} that is the output voltage of the primary full bridge. β_s is the phase angle of U_{ab} that is the input voltage of the secondary full bridge. γ is the phase angle between $U_{AB,1}$ and $U_{ab,1}$, where $U_{AB,1}$ and $U_{ab,1}$ are the fundamental voltage of U_{AB} and U_{ab}, respectively.

The phasor voltages of $U_{AB,1}$ and$U_{ab,1}$ can be derived by the Fourier series expansion, as shown in (1) and (2)

$$\dot{U}_{AB,1} = \frac{2\sqrt{2}}{\pi} V1 \sin\left(\frac{\beta_p}{2}\right) \angle 0 \tag{1}$$

$$\dot{U}_{ab,1} = \frac{2\sqrt{2}}{\pi} V_2 \sin\left(\frac{\beta_s}{2}\right) \angle -\gamma. \tag{2}$$

Fig. 3 shows the equivalent model. U_{ps} and U_{sp} are the induced voltages in the primary and secondary coils, respectively,

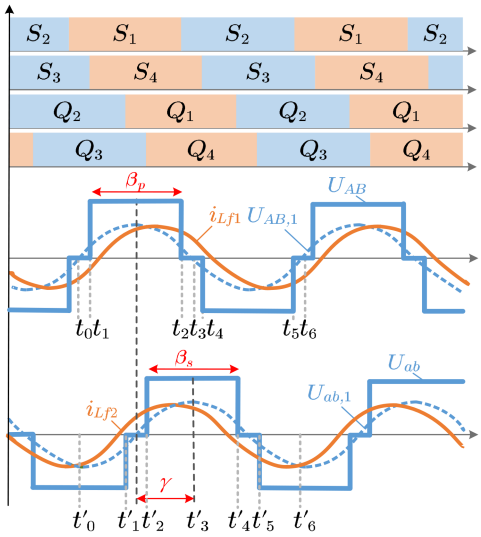

Fig. 2. Waveforms of the WPT system under TPS control.

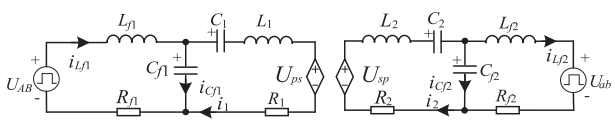

Fig. 3. AC equivalent circuit of *LCC–LCC* compensated WPT system.

and they are given by

$$\dot{U}_{ps} = -j\omega M\dot{I}_2 \tag{3}$$

$$\dot{U}_{sp} = j\omega M\dot{I}_1. \tag{4}$$

If the system is completely resonant, i.e.,

$$\begin{cases} \omega L_{f1} = \frac{1}{\omega C_{f1}}, \omega L_{f2} = \frac{1}{\omega C_{f2}} \\ \omega L_1 - \frac{1}{\omega C_{f1}} = \frac{1}{\omega C_1}, \omega L_2 - \omega L_{f2} = \frac{1}{\omega C_2} \end{cases}.$$

Neglecting the loss resistances and using Kirchhoff's voltage law (KVL), the phase form of the currents i_1, i_2, i_{Lf1}, and i_{Lf2} at the fundamental harmonic frequency can be deduced as follows:

$$\dot{I}_{1,1} = -j\frac{\dot{U}_{AB,1}}{\omega L_{f1}} \tag{5}$$

$$\dot{I}_{2,1} = j\frac{\dot{U}_{ab,1}}{\omega L_{f2}} \tag{6}$$

$$\dot{I}_{Lf1,1} = \frac{M\dot{I}_{2,1}}{L_{f1}} = j\frac{M\dot{U}_{ab,1}}{\omega L_{f1}L_{f2}} \tag{7}$$

$$\dot{I}_{Lf2,1} = \frac{M\dot{I}_{1,1}}{L_{f2}} = -j\frac{M\dot{U}_{AB,1}}{\omega L_{f1}L_{f2}} \tag{8}$$

where $X = \omega L_{f1} = \omega L_{f2}$ is the characteristic impedance of the system.

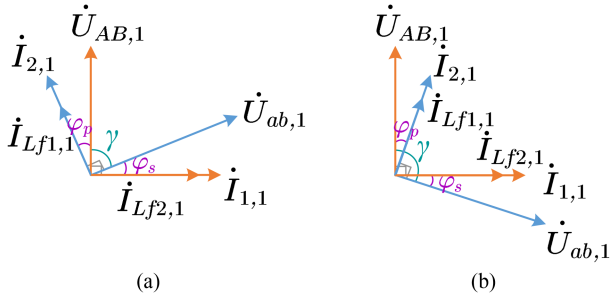

Fig. 4. Vector relationship between voltage and current.

The transferred active power and reactive power are calculated by

$$P_s = \mathrm{Re}\left\{\dot{U}_{ab,1}\dot{I}^*_{Lf2}\right\} = \frac{\sqrt{L_1L_2}}{\omega L_{f1}L_{f2}}k\left|\dot{U}_{ab,1}\right|\left|\dot{U}_{AB,1}\right|\sin(\gamma) \tag{9}$$

$$Q_s = \mathrm{Im}\left\{\dot{U}_{ab,1}\dot{I}^*_{Lf2}\right\} = \frac{\sqrt{L_1L_2}}{\omega L_{f1}L_{f2}}k\left|\dot{U}_{ab,1}\right|\left|\dot{U}_{AB,1}\right|\cos(\gamma). \tag{10}$$

According to (5)–(8), the vector relationship between voltage and current is shown in Fig. 4. φ_p is the phase angle between $U_{AB,1}$ and $i_{Lf1,1}$, and φ_s is the phase angle between $U_{ab,1}$ and $i_{Lf2,1}$. It is clear that the phase angle φ_p and φ_s can be derived as

$$\varphi_p = \begin{cases} \pi/2 - \gamma & 0 \le \gamma \le \pi/2 \\ \gamma - \pi/2 & \pi/2 < \gamma \le \pi \end{cases} \tag{11}$$

$$\varphi_s = \begin{cases} \pi/2 - \gamma & 0 \le \gamma \le \pi/2 \\ \gamma - \pi/2 & \pi/2 < \gamma \le \pi \end{cases}. \tag{12}$$

As can be found from (11) and (12), the phase angles φ_p and φ_s are related to γ, which means φ_p and φ_s can be simultaneously regulated by only changing γ. Therefore, with the variation of γ from 0 to π, the input impedance of the secondary full bridge changes from capacitive to inductive. Meanwhile, the output impedance of the primary full bridge changes from inductive to capacitive. As a result, it is easy to realize soft-switching for primary and secondary full bridges by adjusting γ, which is analyzed in the next section.

B. ZVS Conditions Analysis

It should be emphasized that the hard-switching of power switches is a significant challenge for WPT systems at high-frequency operation. Thus, ZVS operation of both the primary and secondary full bridges is desired.

Although the FHA model is accurate enough for power calculating, it has a nonnegligible error in determining ZVS range due to the high-order harmonics in output currents of full bridges. In order to analyze ZVS conditions, the time domain model of the full-bridge output current needs to be established by taking the harmonics into consideration. The specific derivation process

can be found in [20]. According to [20], the critical phase angle γ for ZVS realization of primary and secondary power switches, respectively, can be derived as

$$\gamma_1 = \frac{\pi}{2} - \frac{\beta_p}{2} + \cos^{-1}\left(\frac{2\pi X I_{ZVS} + V_1\left(\beta_p \pi - 8\sin(\beta_p/2)\right)}{8\lambda k V_2 \sin(\beta_s/2)}\right) \tag{13}$$

$$\gamma_2 = \frac{\pi}{2} - \frac{\beta_s}{2} + \cos^{-1}\left(\frac{2\pi X I_{ZVS} + V_2\left(\beta_s \pi - 8\sin(\beta_s/2)\right)}{8\lambda k V_1 \sin(\beta_p/2)}\right) \tag{14}$$

where $\lambda = L_1/L_{f1} = L_2/L_{f2}$, $X = \omega L_{f1} = \omega L_{f2}$, I_{ZVS} is the threshold current and $I_{ZVS} = 2C_{\text{oss}}U_{dc}/t_{\text{d}}$.

The optimal phase angle γ for ZVS realization of all power switches in both the primary and secondary side can be derived as

$$\gamma = \max(\gamma_1, \gamma_2). \tag{15}$$

C. Conditions for Load-Matching and Maximum Transfer Efficiency of the Resonant Tank

The loss model of the resonant network is built as shown in Fig. 3. R_1 and R_2 are the parasitic resistances of the primary and secondary coils, respectively. R_{Lf1} and R_{Lf2}, are the equivalent loss resistances of the compensation inductors. The losses of the resonant network are given by

$$P_{\text{Loss\_net}} = I_{Lf1}^2 R_{Lf1} + I_1^2 R_1 + I_{Lf2}^2 R_{Lf2} + I_2^2 R_2. \tag{16}$$

Then, the efficiency of resonant network can be given by η_{net}

$$\eta_{\text{net}} = \frac{P_o}{P_{\text{Loss\_net}} + P_o}. \tag{17}$$

Substituting (9) into (17) and assuming $R_1 = R_2 = R_c$ and $R_{Lf1} = R_{Lf2} = R_f$, the efficiency η_{net} can be obtained by

$$\eta_{\text{net}} = \frac{k\lambda X\left|\sin\gamma\right|}{k\lambda X\left|\sin\gamma\right| + (k^2\lambda^2 R_f + R_c)T_{ac} + (k^2\lambda^2 R_f + R_c)\frac{1}{T_{ac}}} \tag{18}$$

where T_{ac} is the ratio of the excitation voltages in the primary and secondary side

$$T_{ac} = \frac{U_{ab,1}}{U_{AB,1}} = \frac{V_2 \sin\left(\frac{\beta_s}{2}\right)}{V_1 \sin\left(\frac{\beta_p}{2}\right)}. \tag{19}$$

Solving the derivative of η_{net} with respect to T_{ac}, the excitation voltage ratio to obtain the maximum efficiency of the resonant tank is derived as

$$\frac{d\eta_{\text{net}}}{dT_{ac}} = 0 \Rightarrow T_{ac} = 1. \tag{20}$$

From (20), it is obvious that in order to obtain the maximum system efficiency, equal primary, and secondary excitation voltages should be implemented. This is the load-matching condition.

According to (19) and (20), β_p and β_s satisfy

$$\beta_p = 2\text{arc}\sin\left(\frac{V_2}{V_1}\sin\left(\frac{\beta_s}{2}\right)\right). \tag{21}$$

TABLE I
ELECTRICAL PARAMETERS OF THE WPT SYSTEM

Symbol	Description	Value
V_1	Input Voltage	400 V
V_2	Output Voltage	100-400 V
f_n	Resonant frequency	85 *k*Hz
L_{f1}	Primary compensation inductance	50 μH
C_{f1}	Primary parallel compensation capacitance	70.4 *n*F
C_1	Primary series compensation capacitance	21 *n*F
L_1	Primary coil inductance	217 μH
M	Mutual inductance in well-aligned case	65.1 μH
k	Coupling coefficient	0.3
L_{f2}	Secondary compensation inductance	50 μH
C_{f2}	Secondary parallel compensation capacitance	70.4 *n*F
C_2	Secondary series compensation capacitance	21 *n*F
L_2	Secondary coil inductance	217 μH

The phase shift angles β_p and β_s are used to realize load matching, namely voltage matching of the excitation voltages. For a given output power P_o, the optimal β_p and β_s can be calculated as

$$\beta_p = 2\arcsin\left(\frac{\pi}{2V_1}\sqrt{\frac{X}{2\lambda k}P_o}\right) \tag{22}$$

$$\beta_s = 2\arcsin\left(\frac{\pi}{2V_2}\sqrt{\frac{X}{2\lambda k}P_o}\right). \tag{23}$$

D. Problem of Unmatched DC Voltages on the Primary and Secondary Sides

A WPT system that operates efficiently over a wide range of output voltages is preferred because it can charge batteries at different voltages. In this article, the primary input voltage is fixed at 400 V and the output voltage varies from 100 to 400 V. The designed maximum transmission power is 6.6 kW for the *LCC–LCC* compensated WPT system. The parameters of magnetic coupler used in this article are $L_1 = L_2 = 217$ μH, mutual inductance $M = 65.1$ μH. These parameters are obtained by multiobjective optimization with an air gap of 140 mm and physical dimensions of 600 mm $\times$ 600 mm. The design method for parameter optimization of magnetic coupling has been provided in previously published paper [37]. With the maximum transmission power, the compensation inductance parameters can be calculated as $L_{f1} = L_{f2} = 50$ μH. Then, the value of C_{f1}, C_{f2}, C_1, and C_2 can be derived according to the resonant conditions. Therefore, we can obtain several important parameters for the proposed converter, organized in Table I.

With the parameters listed in Table I, $\Delta\gamma$ ($\Delta\gamma = \gamma$-$\pi/2$) and β_s as a function of output power P_o are plotted in Fig. 5 according to (15), (22), and (23). We can clearly find that the $\Delta\gamma$ increases as P_o decreases. As shown in Table I, the ratio of output dc voltage to input dc voltage varies from 0.25 to 1. When the dc voltage ratio is not equal to 1, that is, $V_2 < V_1$, β_p and β_s cannot satisfy (20) anymore due to the unmatched dc voltages under heavy load, so β_s is kept 180° to approximate unit excitation voltage ratio and maintain high efficiency. Only when $V_2 = V_1$, (20) can be satisfied over the entire power range.

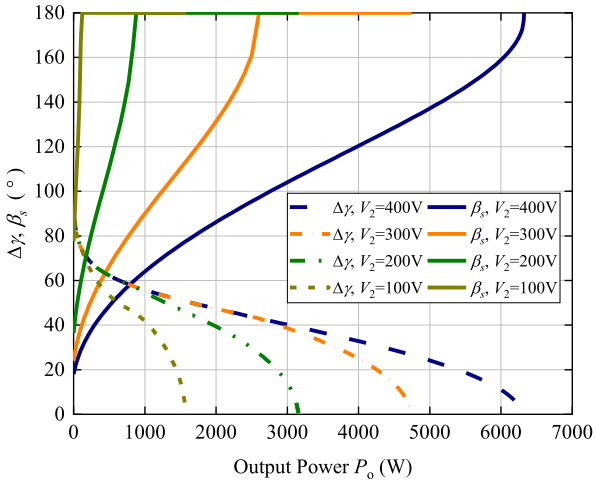

Fig. 5. $\Delta\gamma$ and β_s versus output power for load matching condition and ZVS.

To achieve the load-matching condition, according to (19) we can easily get $\beta_p < \beta_s$ under the condition that $V_2 < V_1$. Then, γ can be calculated by (13), i.e., $\gamma = \gamma_1$. In this case, the primary and secondary MOSFETs can also realize ZVS. However, this TPS method can only achieve ZVS of the primary-side converter with minimum reactive power, but it brings relatively large reactive power to the secondary side. Moreover, the high current stress on the secondary full-bridge input causes large turn-off losses and conduction losses. The above two aspects limit the further efficiency improvement of WPT system.

III. Proposed Method

A control method is proposed in this section to overcome the problem of Section II-D. An SCC is added to the secondary side to adjust the series compensation capacitance. This can ensure a minimum circulating reactive power on both sides and reduce the input current of the rectifier even if V_2 varies widely away from V_1.

This section will introduce the basic concept of the SCC first. Then, the circuit characteristics, including current, output power, and impedance, are analyzed to demonstrate the advantages of the introduction of SCC. Furthermore, the optimal value of adjustable capacitance is derived based on the established time-domain model.

A. Operation of the SCC

A variable compensation capacitor is introduced for *LCC–LCC* compensation topology to improve system efficiency. The circuit diagram is shown in Fig. 6. The secondary-side series compensation capacitor C_2 is not a fixed-value, whereas it is adjustable according to the different loads for achieving a minimum circulating reactive power on both sides and reduce the rectifier input current. The variable C_2 consists of a fixed capacitor C_x, and two MOSFET switches, S_a and S_b, forming an SCC.

The switching sequences and the operating waveforms of the SCC are shown in Fig. 7. S_a is turned OFF with a time delay of

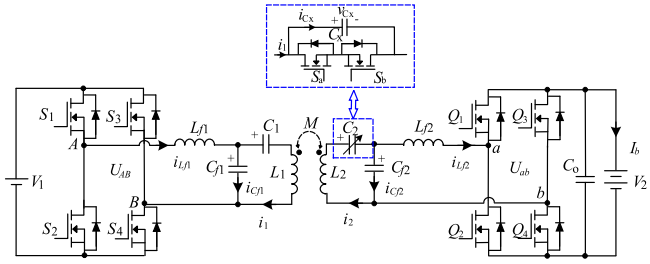

Fig. 6. Proposed *LCC–LCC* compensated WPT system with SCC.

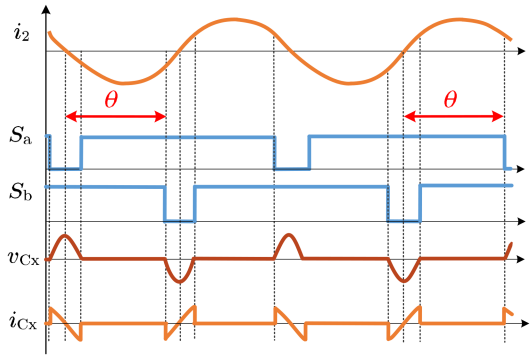

Fig. 7. Operation waveforms of the SCC.

θ to the zero-cross point where i_2 commutates from negative to positive and then turned back ON after another time delay $2\pi - 2\theta$. S_b is turned OFF with a time delay of θ to the zero-cross point where i_2 commutates from positive to negative, and turned back ON after another time delay $2\pi - 2\theta$. With this modulation method of the SCC, when C_x is shorted, the current mainly flows through S_a and S_b rather than through the antiparallel diodes of both of the MOSFETs. Thus, a low conducting loss of the MOSFETs in the SCC can be realized. Meanwhile, since S_a and S_b are turned ON at zero voltage, ZVS can be achieved to minimize the switching losses.

The equivalent capacitance of the SCC can be modulated by varying the control angle θ ($\pi/2 \le \theta \le \pi$). According to the Fourier decomposition of vCx, without considering high-order harmonics, the equivalent adjustable capacitance C_2 can be derived as [27]

$$C_{eq} = \frac{\pi C_X}{2\pi - 2\theta + \sin(2\theta)}. \tag{24}$$

The trend of the ratio C_{eq}/C_x with control angle θ is as shown in Fig. 8. When θ varies from $\pi/2$ to π, the capacitance ratio could range from 1 to $+\infty$ in theory.

B. Circuit Characteristic of LCC/LCC Compensation Topology With Adjustable C2

In this section, we will derive the conditions that variable capacitor C_2 needs to meet to reduce current stress and reactive power. In addition, the effect of C_2 variation on the resonant currents, output power, primary input phase angle φ_p, and secondary output phase angle φ_s is discussed.

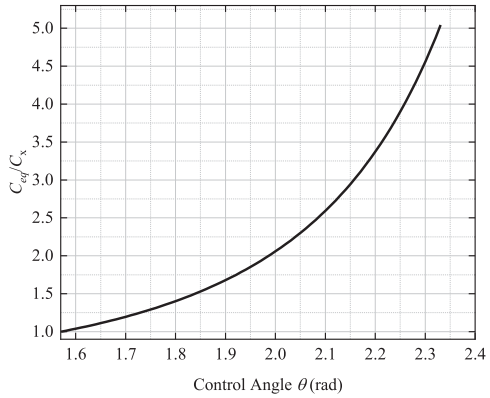

Fig. 8. Relationship between capacitance magnification ratio and the control angle.

1) RMS Current of I_1, I_2, I_{Lf1}, and I_{Lf2}: The transfer efficiency is the most important index for a WPT system and it is directly related to the current RMS, so the variations in the current RMS with adjustable C_2 considered are analyzed here.

First, the equivalent capacitance value of C_2 controlled by SCC is denoted as C_{eq}, and ε is used to express the relationship between C_{eq} and the ideal resonant capacitances C_{2_0}:

$$\varepsilon = \frac{C_{eq}}{C_{2\_0}}. \tag{25}$$

Then, the ratio of the equivalent reactance caused by the change in C_2 to the ideal reactance X can be described as

$$\xi = \frac{\omega L_2 - \frac{1}{\omega C_{eq}}}{X}. \tag{26}$$

ε is introduced to more intuitively discover the variation trend of C_{eq} with respect to C_{2_0}. The introduction of ξ can simplify the formula.

The KVL equations of the proposed system can be obtained as

$$\begin{cases} \dot{U}_{AB} = j\omega L_{f1}\dot{I}_{Lf1} + \left(\dot{I}_{Lf1} - \dot{I}_1\right)/(j\omega C_{f1}) \\ \left(\dot{I}_{Lf1} - \dot{I}_1\right)/(j\omega C_{f1}) = \dot{I}_1/(j\omega C_1) + j\omega L_1\dot{I}_1 - j\omega M\dot{I}_2 \\ j\omega M\dot{I}_1 = \dot{I}_2/(j\omega C_{2eq}) + j\omega L_2\dot{I}_2 + \left(\dot{I}_2 - \dot{I}_{Lf2}\right)/(j\omega C_{f2}) \\ \left(\dot{I}_2 - \dot{I}_{Lf2}\right)/(j\omega C_{f2}) = j\omega L_{f2}\dot{I}_{Lf2} + \dot{U}_{ab} \end{cases}. \tag{27}$$

If varying C_2, the system is not completely resonant, i.e.,

$$\frac{1}{\omega C_{2eq}} \neq \omega(L_2 - L_{f2}). \tag{28}$$

According to the condition of (28), it is found by a derivation that this nonresonance does not change the calculation of currents I_1, I_2, and I_{Lf1}, i.e., (5)–(7) still holds. However, the expression for I_{Lf2} is derived as in (29) after considering the variation of C_2

$$\dot{I}_{Lf2,1\_SCC} = \frac{\omega M\dot{I}_{1,1}}{X} - (\xi - 1)\dot{I}_{2,1}$$

$$= -j\left(\frac{\omega M\dot{U}_{AB,1}}{X^2} + (\xi - 1)\frac{\dot{U}_{ab,1}}{X}\right). \tag{29}$$

The ratio of the RMS I_{Lf2} with the SCC to that of the ideally compensated condition is used to evaluate the effect of C_2 on the RMS I_{Lf2}, that is

$$\frac{\left|\dot{I}_{Lf2,1\_SCC}\right|}{\left|\dot{I}_{Lf2,1}\right|} = \frac{\left|\left(\omega M\dot{U}_{AB,1} + (\xi - 1)X\dot{U}_{ab,1}\right)\right|}{\left|\omega M\dot{U}_{AB,1}\right|}$$

$$= \sqrt{1 + \frac{b^2 + 2ab\cos(\gamma)}{a^2}},$$

$$\text{where} \begin{cases} a = \omega M\left|\dot{U}_{AB,1}\right| \\ b = (\xi - 1)X\left|\dot{U}_{ab,1}\right| \end{cases} \tag{30}$$

where $a > 0$; if $\xi > 1$, $b > 0$.

According to (30), to reduce the RMS I_{Lf2}, it is necessary to satisfy

$$b^2 + 2ab\cos(\gamma) < 0 \Rightarrow 0 < b < -2a\cos(\gamma). \tag{31}$$

The ξ and ε can be deduced as respectively

$$1 < \xi < 1 + \frac{-2\omega M\left|\dot{U}_{AB,1}\right|\cos(\gamma)}{X\left|\dot{U}_{ab,1}\right|} \tag{32}$$

$$1 < \varepsilon < \frac{1}{1 + \frac{2\omega^2 C_{2\_0} M\left|\dot{U}_{AB,1}\right|\cos(\gamma)}{\left|\dot{U}_{ab,1}\right|}}. \tag{33}$$

According to the above-mentioned derivation, the current I_{Lf2} can be decreased by adjusting $\varepsilon > 1$. The equivalent capacitance C_{eq} adjusted by SCC needs to be larger than the ideal resonant capacitance value to reduce the current stress on the active rectifier. In addition, I_1, I_2, and I_{Lf1} are independent of ε. Adjusting the equivalent capacitance of the SCC can reduce the current stress of the active rectifier without increasing the other resonant currents RMS, which reduces the turn-ON and turn-OFF losses.

2) Output Power: For a WPT system, a stable and controllable output power is desired. The output power under the ideal compensation condition is calculated according to (9). When C_2 is regulated by SCC, with a detailed derivation, the output power can be calculated as follows:

$$P_s = \mathrm{Re}\left\{\dot{U}_{ab,1}\dot{I}^*_{Lf2}\right\} = \frac{M\left|\dot{U}_{AB,1}\right|\left|\dot{U}_{ab,1}\right|\sin(\gamma)}{L_{f1}L_{f2}}. \tag{34}$$

From (34), it can be seen that the output active power is independent of ε. Equation (34) is consistent with (9). This means that the output power remains constant under varying C_2.

Although the proposed control method adds an additional control variable θ when SCC is introduced, it does not increase the complexity of the control.

3) Phase Angle Between $U_{AB,1}$ and $i_{Lf1,1}$: According to the previous analysis, varying C_2 has no effect on the calculation of $I_{Lf1,1}$, i.e., (7) still holds, and therefore, the phase angle

φ_p between $U_{AB,1}$ and $i_{Lf1,1}$ still satisfies (11). This shows that the regulation of C_2 by SCC does not change the input impedance angle, so the ZVS condition of the primary side converter remains unchanged under C_2 regulation.

In the above-mentioned analysis, we conclude that the power and phase angle φ_p remain unchanged when C_2 changes. Although this conclusion is derived using the FHA model, the effect of the change in C_2 on the power and the ZVS condition of the primary side converter can be ignored after considering the higher harmonics.

4) Phase Angle Between $U_{ab,1}$ and $i_{Lf2,1}$: When C_2 is regulated by SCC, the input impedance of the active rectifier can be calculated as follows:

$$Z_s = \frac{\dot{U}_{ab,1}}{\dot{I}_{Lf2,1}} = \frac{\dot{U}_{ab,1}}{-j\left(\frac{\omega M \dot{U}_{AB,1}}{X^2} + (\xi-1)\frac{\dot{U}_{ab,1}}{X}\right)}. \tag{35}$$

Then the phase angle φ_s between $U_{ab,1}$ and $i_{Lf2,1}$ can be obtained as (34)

$$\tan\varphi_s = \frac{\mathrm{Im}(Z_s)}{\mathrm{Re}(Z_s)} = \frac{\omega M \left|\dot{U}_{AB,1}\right| \cos(\gamma) + (\xi-1)X\left|\dot{U}_{ab,1}\right|}{\omega M \left|\dot{U}_{AB,1}\right| \sin(\gamma)}. \tag{36}$$

According to the analysis in Section II, in order to achieve ZVS for all power switches, γ satisfies $\pi/2 \le \gamma \le \pi$, so $\cos(\gamma) \le 0$. From (36), it can be seen that if $\xi > 1$, the φ_s decreases as ξ increases, and when $\xi = 1 - (\omega M|\dot{U}_{AB,1}|\cos(\gamma))/(X|\dot{U}_{ab,1}|)$, $\varphi_s = 0$, the unit-power-factor rectifier can be achieved. Therefore, using SCC to adjust the equivalent capacitance value of C_2 according to (37) is an available way to reduce the φ_s and even achieve active rectifier ZPA

$$1 < \xi \le 1 + \frac{-\omega M \left|\dot{U}_{AB,1}\right| \cos(\gamma)}{X\left|\dot{U}_{ab,1}\right|}. \tag{37}$$

By comparing (32) with (37), it can be seen that (37) is a subset of (32). Therefore, as long as (37) is satisfied, not only the current stress can be reduced, but also the phase angle φ_s can be decreased, thus reducing the reactive power. It is worth noting that if the equivalent capacitance value of C_2 is tuned to $1 - (\omega M|\dot{U}_{AB,1}|\cos(\gamma))/(X|\dot{U}_{ab,1}|)$ according to (37), although minimum current stress and ZPA of the active rectifier can be achieved, ZVS is not guaranteed. This is due to the fact that at light loads, the secondary phase shift angle β_s needs to be modulated, and in this case, the secondary MOSFETs suffer from hard switching, and thus the switching losses increase. Therefore, in this article, the equivalent capacitance value of C_2 is controlled to achieve ZVS for the secondary MOSFETs with minimum reactive power. In this way, the efficiency of the system is maximized.

C. Capacitor Tuning for the Secondary MOSFETs With Minimum Reactive Power

According to the above-mentioned analysis, the efficiency improvement can only be maximized by adjusting C_2 to minimize the reactive power. To determine the value of ε for ZVS realization with minimum reactive power at different loads, a harmonic-based time domain system model is established.

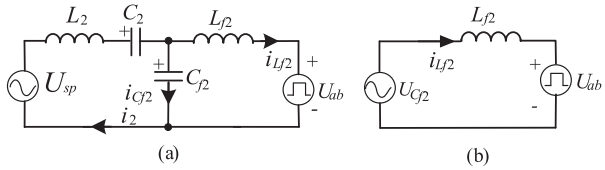

Fig. 9. Simplified circuit model considering high-order harmonics.

Although the FHA model is accurate enough for power calculating, it has a nonnegligible error in determining ε for ZVS realization due to the high-order harmonics in output currents of full bridges. To solve this problem, a time-domain model considering high-order harmonics is developed as shown in Fig. 9(a). Due to the filtering function of L_{f2} and C_{f2}, there are rarely high-order harmonics in the coil current. So the coil current can be calculated by the FHA model instead of a precise model for simplification.

The steady-state waveforms of coil currents calculated by the FHA method are as

$$i_1(t) = \frac{4}{\pi}\frac{V_1}{X}\sin\left(\frac{\beta_p}{2}\right)\sin\left(\omega t - \frac{\pi}{2}\right) \tag{38}$$

$$i_2(t) = \frac{4}{\pi}\frac{V_2}{X}\sin\left(\frac{\beta_s}{2}\right)\sin\left(\omega t - \Delta\gamma\right) \tag{39}$$

where $\Delta\gamma = \gamma$-$\pi/2$.

Then, the time domain expression of the voltage across C_{f2} is derived as (40)

$$u_{Cf2}(t) = \frac{4}{\pi}\lambda k V_1 \sin\left(\frac{\beta_p}{2}\right)\sin(\omega t) - \frac{4}{\pi}\xi V_2 \sin\left(\frac{\beta_s}{2}\right)\cos\left(\omega t - \Delta\gamma\right). \tag{40}$$

So the circuit model can be further simplified with the derived voltage on C_{f2}, as shown in Fig. 9(b). The model can be described with only a differential equation, as shown in the following equation:

$$U_{ab}(t) - U_{Cf2}(t) = -L_{f2}\frac{dI_{Lf2}(t)}{dt}. \tag{41}$$

By solving the differential equations, the expression of the current i_{Lf2} can be derived.

When $t_0' < t < t_1'$, $U_{ab}(t) = -V_2$ and the i_{Lf2} can be derived as

$$i_{Lf2}(t) = i_{Lf2}(t_0') + \frac{V_2}{X}(\omega t - \Delta\gamma) - \frac{4V_2}{\pi X}\xi \times \sin\left(\frac{\beta_s}{2}\right)\sin(\omega t - \Delta\gamma) - \frac{4\lambda k V_1}{\pi X}\sin\left(\frac{\beta_p}{2}\right)\left[\cos(\omega t) - \cos(\Delta\gamma)\right]. \tag{42}$$

When $t_1' < t < t_2'$, $U_{ab}(t) = 0$ the current i_{Lf2} is calculated as

$$i_{Lf2}(t) = i_{Lf2}(t_1') - \frac{4V_2}{\pi X}\xi \sin\left(\frac{\beta_s}{2}\right)$$

$$\times\left[\sin\left(\omega t-\Delta\gamma\right)-\sin\left(\frac{\beta_s}{2}\right)\right]$$
$$-\frac{4\lambda kV_1}{\pi X}\sin\left(\frac{\beta_p}{2}\right)\left[\cos(\omega t)-\cos\left(\frac{\beta_s}{2}+\Delta\gamma\right)\right]. \tag{43}$$

When $t_2'<t<t_3'$, $U_{ab}(t)=V_2$ the current i_{Lf2} is calculated as

$$i_{Lf2}(t)=i_{Lf2}\left(t_2'\right)-\frac{V_2}{X}\left(\omega t-\frac{2\pi-\beta_s}{2}-\Delta\gamma\right)$$
$$-\frac{4V_2}{\pi X}\xi\sin\left(\frac{\beta_s}{2}\right)$$
$$\times\left[\sin(\omega t-\Delta\gamma)-\sin\left(\frac{\beta_s}{2}\right)\right]-\frac{4\lambda kV_1}{\pi X}$$
$$\times\ \sin\left(\frac{\beta_p}{2}\right)\left[\cos(\omega t)+\cos\left(\frac{\beta_s}{2}-\Delta\gamma\right)\right]. \tag{44}$$

Due to the symmetry of the current waveforms, it is obvious

$$i_{Lf2}\left(t_3'=\frac{\pi+\Delta\gamma}{\omega}\right)=-i_{Lf2}\left(t_0'=\frac{\Delta\gamma}{\omega}\right). \tag{45}$$

Then the current i_{Lf2} in t_0' is calculated as

$$i_{Lf2}\left(t_0'\right)=-\frac{4\lambda kV_1}{\pi X}\sin\left(\frac{\beta_p}{2}\right)\cos(\Delta\gamma). \tag{46}$$

With the start point current value, current waveform within the entire switching period can be described analytically.

To realize ZVS operation for active rectifier, energy stored in the parasitic capacitances of switches should be depleted before switches are turned ON. The following constraints should be satisfied:

$$i_{Lf2}(t_1')>I_{ZVS}, i_{Lf2}(t_2')>I_{ZVS} \tag{47}$$

where I_{ZVS} is the threshold current and $I_{ZVS}=2C_{\rm oss}V_1/t_{\rm d}$.

Using the time domain model, the current i_{Lf2} in switching points t_1' and t_2' are calculated as (48) and (49)

$$i_{Lf2}(t_1')=\frac{V_2}{X}\frac{\beta_s}{2}-\frac{4\xi V_2}{\pi X}\sin^2\left(\frac{\beta_s}{2}\right)$$
$$-\frac{4\lambda kV_1}{\pi X}\sin\left(\frac{\beta_p}{2}\right)\cos\left(\frac{\beta_s}{2}+\Delta\gamma\right) \tag{48}$$
$$i_{Lf2}(t_2')=\frac{V_2}{X}\frac{\beta_s}{2}-\frac{4\xi V_2}{\pi X}\sin^2\left(\frac{\beta_s}{2}\right)$$
$$+\frac{4\lambda kV_1}{\pi X}\sin\left(\frac{\beta_p}{2}\right)\cos\left(\frac{\beta_s}{2}-\Delta\gamma\right). \tag{49}$$

If $i_{Lf2}(t_1')>I_{ZVS}$, $i_{Lf2}(t_2')>I_{ZVS}$ must be satisfied since $i_{Lf2}(t_2')>i_{Lf2}(t_1')$. So with only $i_{Lf2}(t_1')>I_{ZVS}$, ZVS operation of all secondary side switches can be ensured.

According to the previous analysis, in order to achieve high-efficiency modulation, SCC is used to control the equivalent capacitance value of C_2 to realize ZVS with the minimum reactive power on both sides. In order to realize this goal, the current at the switching point should be controlled at the minimum value,

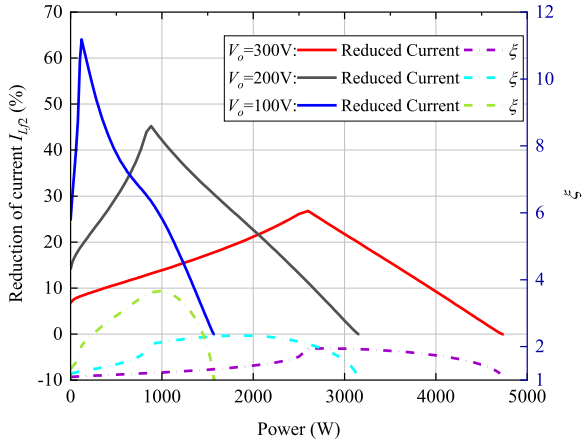

Fig. 10. Variation of reduction of current I_{Lf2} and ξ with power.

i.e., $i_{Lf2}(t_1')=I_{ZVS}$. By solving (48) with switching current I_{ZVS}, the optimal ξ can be derived as

$$\xi_{\rm opt}=-\frac{2\pi XI_{ZVS}-\pi V_2\beta_s+8\lambda kV_1\sin\left(\frac{\beta_p}{2}\right)\cos\left(\frac{\beta_s}{2}+\Delta\gamma\right)}{8V_2\sin^2\left(\frac{\beta_s}{2}\right)}. \tag{50}$$

From (50), it can be seen that when the voltages V_1 and V_2 are defined, ξ can be calculated according to the phase shift angles β_p, β_s, and $\Delta\gamma$ at any power. The trend of ξ with output power for different output voltages is shown in Fig. 10. It can be seen that the lower the output voltage, the larger the range of variation of ξ over the full power range, and the value of ξ is close to 1 for both heavy and light loads. In addition, Fig. 10 describes the reduction of current I_{Lf2} relative to $\xi=1$ with the change of ξ. As can be seen, the maximum current drop of I_{Lf2} can be up to 27%, 45%, and 64% at output voltages of 300, 200, and 100 V, respectively, over the whole power range. This demonstrated that by adjusting the equivalent capacitance value of C_2 according to (50), not only the ZVS on the secondary side can be achieved with minimum reactive power, but also the current stress can be reduced, thus increasing the efficiency.

According to (26), the optimal ε is derived as

$$\varepsilon_{\rm opt}=1/(\omega C\left(\omega L_1-\xi_{\rm opt}X\right)). \tag{51}$$

Based on the relationship between the control angle θ and ε in (24), the control angle θ of the SCC can be obtained for maximizing efficiency.

IV. Proposed Control Strategy

The block diagram of the proposed control strategy is illustrated in Fig. 11, which contains three subsystems.

1) Controller for primary side.
2) Controller for secondary side.
3) Communications between primary and secondary controllers.

The secondary side control is designed to carry out SCC control and output current or voltage tracking. The adjustment of β_s and the phase synchronization between two sides is used for

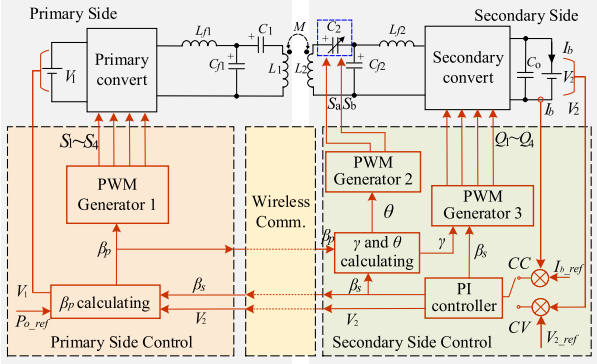

Fig. 11. Diagram of the proposed control strategy.

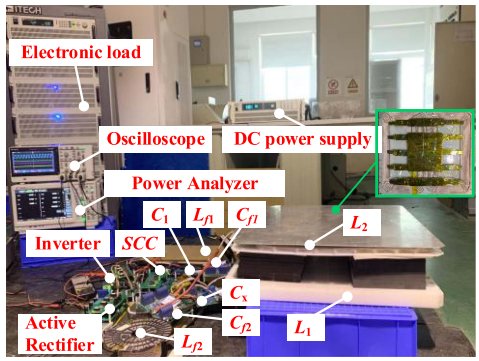

Fig. 12. Experimental setup of the *LCC–LCC* WPT system.

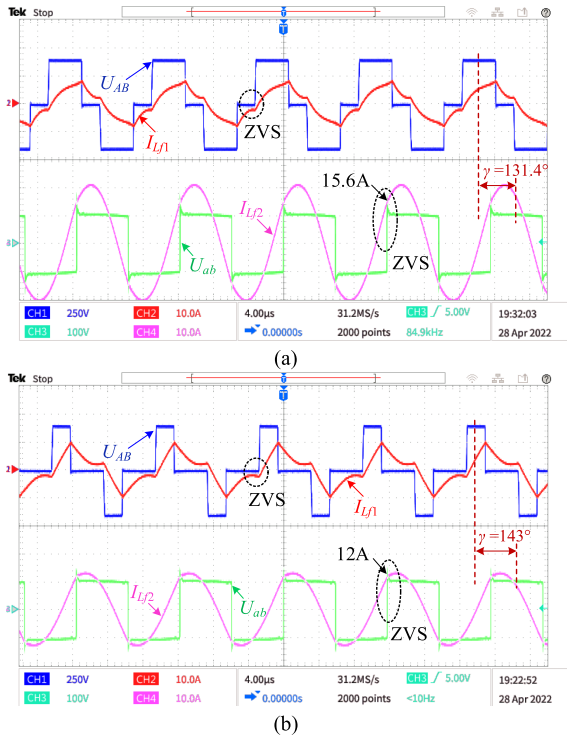

Fig. 13. Output voltage and current waveforms of primary and secondary side bridge under the TPS control without SCC at (a) 1000 W and (b) 500 W.

regulating the output current or voltage to follow the reference values (I_{b_ref} or V_{2_ref}). When the WPT system operates at the CV output mode, at the steady state, the output voltage is maintained at the desired value, and the reactive power on both sides is minimized and ZVS is guaranteed. If a load change occurs on the secondary side, it will cause a voltage deviation, e.g., $V_2 < V_{2\_\mathrm{ref}}$. Then, the PI controller for the active rectifier will increase β_s in order to boost up the output voltage. The primary side control adjusts β_p for load-matching optimization according to β_s. The value of γ varies with the βp and βs to guarantee the ZVS operation on both sides. Then, the SCC control angle θ can be adjusted according to βp, βs, and γ for realizing minimum reactive power and low current stress. As a result, the efficiency optimization, as well as constant voltage, will be efficiently achieved by controlling these four variables. Similar processes in constant current charging mode. The measured battery voltage V_2 and the control signals need to be transmitted via a wireless communication channel.

Phase synchronization between the two controllers on the primary and secondary sides is necessary. Some available solutions can be used to solve this phase-synchronization problem [38], [39]. A more simple and practical method is proposed based on disturbance observation for phase synchronization [40], [41]. According to the relationship between the output current and the relative phase-shift angle γ, the phase synchronization state can be realized by tracking the extreme value of the output current. Disturbance is applied to the γ. If the output current increases, γ will continue to increase or decrease in the same direction. Otherwise, it will change in the opposite direction. With this strategy, the WPT system works well without auxiliary hardware and is independent of the accurate phase difference measurement.

V. Experimental Verification

A. System Setup

An experimental prototype with 400 V input voltage and 100 V output voltage was configured to verify the feasibility of the proposed method, as shown in Fig. 12, which includes a dc power source, an HF inverter, *LCC* resonant networks, an active rectifier, and an electronic load. Two coils of DD structure are employed as the magnetic coupler. Additionally, the efficiency of the WPT system is measured by the power analyzer ZLG PA8000. DSP TMS320F28335 is employed to implement the digital controller. More detailed system parameters are given in Table I.

B. Steady-State Waveforms

Figs. 13 and 14 show the experimental results of TPS without SCC and the proposed control under different power.

It can be seen from Figs. 13 and 14 that both TPS without SCC and the proposed control can realize ZVS on both primary and secondary side at different powers. For TPS without SCC, as shown in Fig. 13, when the output power is 1000 and 500 W, the turn-off current I_{off} is 15.6 and 12 A, respectively. As a

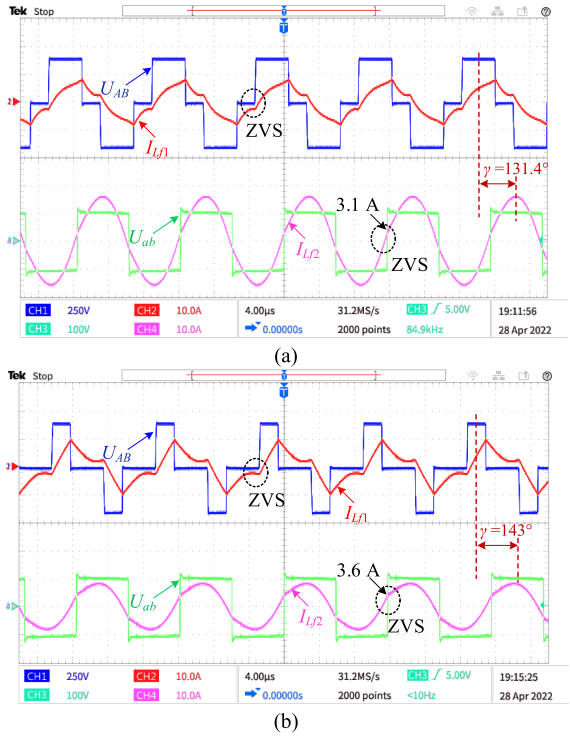

Fig. 14. Output voltage and current waveforms of primary and secondary side bridge with the proposed control strategy at (a) 1000 W and (b) 500 W.

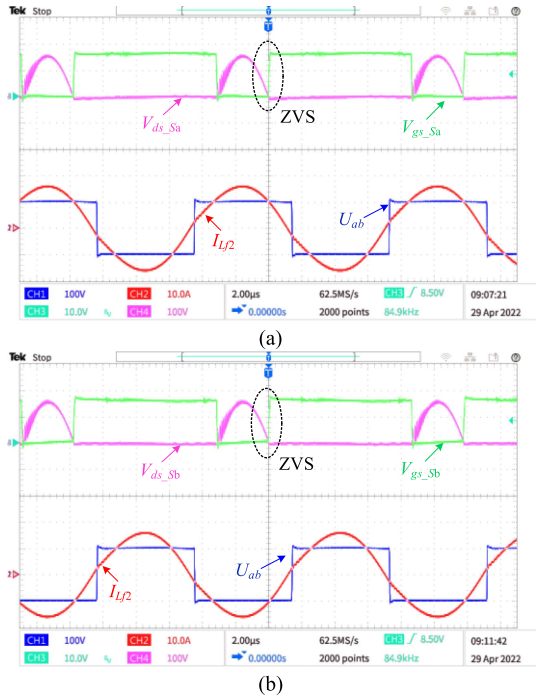

Fig. 15. ZVS condition of the MOSFETs in SCC. (a) S_a. (b) S_b.

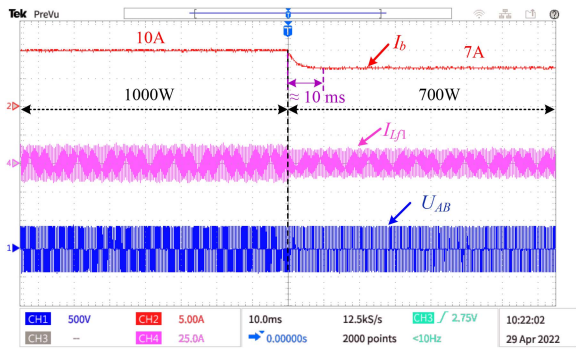

Fig. 16. Dynamic process when I_b varies from 10 to 7 A with a constant output voltage $V_2 = 100$ V.

result, with the TPS without SCC, both the turn-off loss and the reactive power loss increase, which will degrade the system efficiency.

However, for the proposed control, as shown in Fig. 14, when the output power is 1000 and 500 W, the I_{off} remains around 3.5 A, which is in accordance with the theoretical analysis. Thus, the turn-off loss decreases significantly and the reactive power loss can be minimized with the proposed control. In addition, comparing Figs. 13 and 14, it can be seen that under the proposed method, the RMS current of i_{Lf2} is lower than that of TPS without SCC, which results in a smaller conduction loss. This verifies the effectiveness of the proposed method.

To verify that both MOSFETs in the SCC can achieve ZVS, the experimental results are shown in Fig. 15. It can be seen that the voltage across the drain and source of the MOSFET reaches zero before the gating signal switches to high, which proves the ZVS can be achieved in both S_a and S_b of the SCC.

C. Dynamic Performance

In order to verify the dynamic performance of the proposed control, the prototype is tested under step variation of the output current. The results are shown in Fig. 16. It shows the waveforms of the dynamic process when I_b varies from 10 to 7 A with a constant output voltage $V_2 = 100$ V. That is, the output power changes from 1000 to 700 W. The transient response time is about 10 ms, which is fast enough for hourly charging time.

D. Efficiencies and Power Losses

The measured dc to dc efficiency with two control strategies at different power level are shown in Fig. 17. All efficiency data results presented in Fig. 17 are measured using the power analyzer ZLG PA8000. With these two control strategies, the efficiencies were measured at different powers with the same measurement method and measuring instruments. It can be found that the efficiency with the proposed TPS+SCC control is higher than that with TPS control only over the whole output power range, which is due to the fact that ZVS is achieved with minimum reactive current on both sides and the RMS current of i_{Lf2} is reduced, so that the turn-off loss, the reactive power loss, and the conduction loss are all reduced. At 700 W, efficiency can be improved up to 1.7%. Given the EVs' charging time lasting for hours, the saved energy is considerable, which holds great potential in the case of high-power charging.

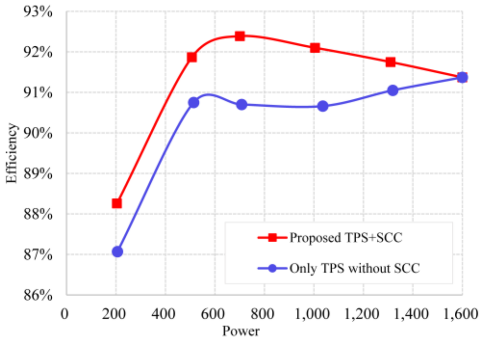

Fig. 17. Efficiency versus the output power.

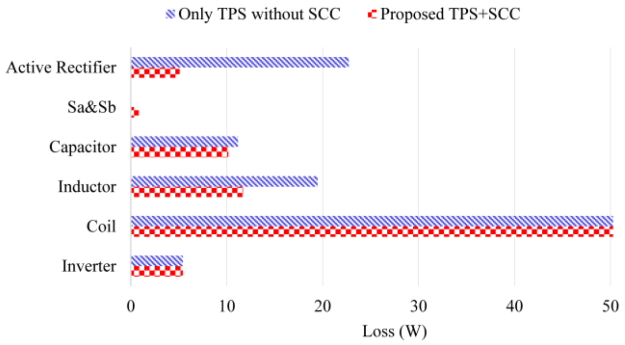

Fig. 18. Losses breakdown analysis with two control strategies at 1000 W.

The loss of each component in the WPT system has been analyzed through theoretical calculations and shown in Fig. 18, which depicts various losses of the prototype system with two control methods at 1000 W output. In the proposed TPS control strategy with SCC, the power loss of the SCC is very low because ZVS is achieved and the turn-off loss can be ignored referring to Fig. 15. The coil loss accounts for the largest proportion under both control strategies. Under the proposed TPS+SCC control strategy, although additional power losses caused by the SCC are unavoidable, the power losses of the active rectifier and inductor can be reduced significantly compared with TPS only. The power losses in the inverter and coils are similar under both control strategies.

VI. Conclusion and Discussion

In order to improve the efficiency of the WPT system with wide output voltage, a practical control strategy is proposed with TPS combined with SCC for *LCC–LCC* compensated WPT system. The introduction of SCC can solve the high reactive power problem under the TPS control method for a wide voltage output system. With the proposed control method, the reactive power can be minimized on both the primary and the secondary sides, and the input current stress of the rectifier can be low without affecting other circuit characteristics. With the proposed method, the overall efficiency can be improved compared to the WPT system with TPS control owing to the minimized reactive power and low turn-off and conduction losses. A laboratory prototype is built to verify the effectiveness of the proposed control method. Experimental results indicate that the system with the proposed control technique achieves a higher efficiency over the TPS within the entire power range.

References

[1] C. C. Mi, G. Buja, S. Y. Choi, and C. T. Rim, "Modern advances in wireless power transfer systems for roadway powered electric vehicles," *IEEE Trans. Power Electron.*, vol. 63, no. 10, pp. 6533–6545, Oct. 2016.

[2] H. Feng, R. Tavakoli, O. C. Onar, and Z. Pantic, "Advances in high-power wireless charging systems: Overview and design considerations," *IEEE Trans. Power Electron.*, vol. 6, no. 3, pp. 886–919, Sep. 2020.

[3] H. T. Nguyen et al., "Review map of comparative designs for wireless high-power transfer systems in EV applications: Maximum efficiency, ZPA, and CC/CV modes at fixed resonance frequency independent from coupling coefficient," *IEEE Trans. Power Electron.*, vol. 37, no. 4, pp. 4857–4876, Apr. 2022.

[4] L. Zhao, D. J. Thrimawithana, U. K. Madawala, A. P. Hu, and C. C. Mi, "A misalignment-tolerant series-hybrid wireless EV charging system with integrated magnetics," *IEEE Trans. Power Electron.*, vol. 34, no. 2, pp. 1276–1285, Feb. 2019.

[5] X. Qu, H. Han, S. C. Wong, C. K. Tse, and W. Chen, "Hybrid IPT topologies with constant current or constant voltage output for battery charging applications," *IEEE Trans. Power Electron.*, vol. 30, no. 11, pp. 6329–6337, Nov. 2015.

[6] V. B. Vu, D. H. Tran, and W. Choi, "Implementation of the constant current and constant voltage charge of inductive power transfer systems with the double-sided LCC compensation topology for electric vehicle battery charge applications," *IEEE Trans. Power Electron.*, vol. 33, no. 9, pp. 7398–7410, Sep. 2018.

[7] H. Li, J. Li, K. Wang, W. Chen, and X. Yang, "A maximum efficiency point tracking control scheme for wireless power transfer systems using magnetic resonant coupling," *IEEE Trans. Power Electron.*, vol. 30, no. 7, pp. 3998–4008, Jul. 2015.

[8] T. Orekan, P. Zhang, and C. Shih, "Analysis, design, and maximum power-efficiency tracking for undersea wireless power transfer," *IEEE J. Emerg. Sel. Topics Power Electron.*, vol. 6, no. 2, pp. 843–854, Jun. 2018.

[9] K. Song et al., "Constant current charging and maximum system efficiency tracking for wireless charging systems employing dual-side control," *IEEE Trans. Ind. Appl.*, vol. 56, no. 1, pp. 622–634, Jan./Feb. 2020.

[10] Y. Jiang, L. Wang, J. Fang, C. Zhao, K. Wang, and Y. Wang, "A joint control with variable ZVS angles for dynamic efficiency optimization in wireless power transfer system," *IEEE Trans. Power Electron.*, vol. 35, no. 10, pp. 11064–11081, Oct. 2020.

[11] S. Ann and B. K. Lee, "Analysis of impedance tuning control and synchronous switching technique for a semibridgeless active rectifier in inductive power transfer systems for electric vehicles," *IEEE Trans. Power Electron.*, vol. 36, no. 8, pp. 8786–8798, Aug. 2021.

[12] B. X. Nguyen et al., "An efficiency optimization scheme for bidirectional inductive power transfer systems," *IEEE Trans. Power Electron.*, vol. 30, no. 11, pp. 6310–6319, Nov. 2015.

[13] Z. Huang, S. C. Wong, and C. K. Tse, "An inductive-power-transfer converter with high efficiency throughout battery-charging process," *IEEE Trans. Power Electron.*, vol. 34, no. 10, pp. 10245–10255, Oct. 2019.

[14] C.-S. Wang, G. A. Covic, and O. H. Stielau, "Power transfer capability and bifurcation phenomena of loosely coupled inductive power transfer systems," *IEEE Trans. Power Electron.*, vol. 51, no. 1, pp. 148–157, Feb. 2004.

[15] Y. Li, J. Hu, F. Chen, Z. Li, Z. He, and R. Mai, "Dual-phase-shift control scheme with current-stress and efficiency optimization for wireless power transfer systems," *IEEE Trans. Circuits Syst. I, Reg. Papers*, vol. 65, no. 9, pp. 3110–3121, Sep. 2018.

[16] R. Mai, Y. Liu, Y. Li, P. Yue, G. Cao, and Z. He, "An active-rectifier-based maximum efficiency tracking method using an additional measurement coil for wireless power transfer," *IEEE Trans. Power Electron.*, vol. 33, no. 1, pp. 716–728, Jan. 2018.

[17] M. Wu et al., "A dual-sided control strategy based on mode switching for efficiency optimization in wireless power transfer system," *IEEE Trans. Power Electron.*, vol. 36, no. 8, pp. 8835–8848, Aug. 2021.

[18] Y. Jiang et al., "Phase-locked loop combined with chained trigger mode used for impedance matching in wireless high power transfer," *IEEE Trans. Power Electron.*, vol. 35, no. 4, pp. 4272–4285, Apr. 2020.

[19] S. Chen et al., "An operation mode selection method of dual-side bridge converters for efficiency optimization in inductive power transfer," *IEEE Trans. Power Electron.*, vol. 35, no. 10, pp. 9992–9997, Oct. 2020.
[20] X. Zhang et al., "A control strategy for efficiency optimization and wide ZVS operation range in bidirectional inductive power transfer system," *IEEE Trans. Ind. Electron.*, vol. 66, no. 8, pp. 5958–5969, Aug. 2019.
[21] S. Li, W. Li, J. Deng, T. D. Nguyen, and C. C. Mi, "A double-sided LCC compensation network and its tuning method for wireless power transfer," *IEEE Trans. Veh. Technol.*, vol. 64, no. 6, pp. 2261–2273, Jun. 2015.
[22] T. Kan, T.-D. Nguyen, J. C. White, R. K. Malhan, and C. C. Mi, "A new integration method for an electric vehicle wireless charging system using LCC compensation topology: Analysis and design," *IEEE Trans. Power Electron.*, vol. 32, no. 2, pp. 1638–1650, Feb. 2017.
[23] W. J. Gu and K. Harada, "A new method to regulate resonant converters," *IEEE Trans. Power Electron.*, vol. 3, no. 4, pp. 430–439, Oct. 1988.
[24] Z. Hu, Y. Qiu, and Y. F. Liu, "Digital implementation of load sharing method for interleaved LLC converters," in *Proc. Control Model. Power Electron.*, 2013, pp. 1–7.
[25] J. Zhang, J. Zhao, Y. Zhang, and F. Deng, "A wireless power transfer system with dual switch-controlled capacitors for efficiency optimization," *IEEE Trans. Power Electron.*, vol. 35, no. 6, pp. 6091–6101, Jun. 2020.
[26] W. Li, Q. Zhang, C. Cui, and G. Wei, "A self-tuning S/S compensation WPT system without parameter recognition," *IEEE Trans. Ind. Electron.*, vol. 69, no. 7, pp. 6741–6750, Jul. 2022.
[27] D.-H. Kim and D. Ahn, "Self-tuning LCC inverter using PWM-controlled switched capacitor for inductive wireless power transfer," *IEEE Trans. Ind. Electron.*, vol. 66, no. 5, pp. 3983–3992, May 2019.
[28] X. Wang, J. Xu, H. Ma, and S. He, "Inductive power transfer systems with digital switch-controlled capacitor for maximum efficiency point tracking," *IEEE Trans. Ind. Electron.*, vol. 68, no. 10, pp. 9467–9480, Oct. 2021.
[29] X. Zhang, J. Li, and X. Tong, "A unique design approach of double-sided LCC compensated IPT system for misalignment-tolerant characteristic," *IEEE Trans. Power Electron.*, vol. 38, no. 1, pp. 1288–1300, Jan. 2023.
[30] X. Wang, J. Xu, M. Leng, H. Ma, and S. He, "A hybrid control strategy of LCC-S compensated WPT system for wide output voltage and ZVS range with minimized reactive current," *IEEE Trans. Ind. Electron.*, vol. 68, no. 9, pp. 7908–7920, Sep. 2021.
[31] U. D. Kavimandan, S. M. Mahajan, and C. W. Van Neste, "Analysis and demonstration of a dynamic ZVS angle control using a tuning capacitor in a wireless power transfer system," *IEEE J. Emerg. Sel. Topics Power Electron.*, vol. 9, no. 2, pp. 1876–1890, Apr. 2021.
[32] K. Song et al., "A control strategy for wireless EV charging system to improve weak coupling output based on variable inductor and capacitor," *IEEE Trans. Power Electron.*, vol. 37, no. 10, pp. 12853–12864, Oct. 2022.
[33] W. Li, G. Wei, C. Cui, X. Zhang, and Q. Zhang, "A double-side self-tuning LCC/S system using a variable switched capacitor based on parameter recognition," *IEEE Trans. Ind. Electron.*, vol. 68, no. 4, pp. 3069–3078, Apr. 2021.
[34] Z. Luo, Y. Zhao, M. Xiong, X. Wei, and H. Dai, "A self-tuning LCC/LCC system based on switch-controlled capacitors for constant-power wireless electric vehicle charging," *IEEE Trans. Ind. Electron.*, vol. 70, no. 1, pp. 709–720, Jan. 2023.
[35] H. Zhang, Y. Chen, C.-H. Jo, S.-J. Park, and D.-H. Kim, "DC-link and switched capacitor control for varying coupling conditions in inductive power transfer system for unmanned aerial vehicles," *IEEE Trans. Power Electron.*, vol. 36, no. 5, pp. 5108–5120, May 2021.
[36] L. Zhou, R. Mai, S. Liu, Y. Li, J. Yu, and L. Fu, "Minimizing input current of the rectifier of LCC–LCC compensated IPT systems by switch-controlled capacitor for improving efficiency," *IEEE Trans. Ind. Appl.*, vol. 58, no. 1, pp. 1010–1021, Jan./Feb. 2022.
[37] J. Deng, W. Li, T. D. Nguyen, S. Li, and C. C. Mi, "Compact and efficient bipolar coupler for wireless power chargers: Design and analysis," *IEEE Trans. Power Electron.*, vol. 30, no. 11, pp. 6130–6140, Nov. 2015.
[38] D. J. Thrimawithana, U. K. Madawala, and M. Neath, "A synchronization technique for bidirectional WPT systems," *IEEE Trans. Ind. Electron.*, vol. 60, no. 1, pp. 310–317, Jan. 2013.
[39] Y. Tang, Y. Chen, U. K. Madawala, D. J. Thrimawithana, and H. Ma, "A new controller for bidirectional wireless power transfer systems," *IEEE Trans. Power Electron.*, vol. 33, no. 10, pp. 9076–9087, Oct. 2018.
[40] T. Tan, K. Chen, Y. Jiang, Q. Lin, L. Yuan, and Z. Zhao, "A bidirectional wireless power transfer system control strategy independent of real-time wireless communication," *IEEE Trans. Ind. Appl.*, vol. 56, no. 2, pp. 1587–1598, Mar./Apr. 2020.
[41] F. Liu, K. Li, K. Chen, and Z. Zhao, "A phase synchronization technique based on perturbation and observation for bidirectional wireless power transfer system," *IEEE J. Emerg. Sel. Topics Power Electron.*, vol. 8, no. 2, pp. 1287–1297, Jun. 2020.

Na Fu received the B.S. degree in measurement & control technology and instrumentation from the Hebei University of Technology, Tianjin, China, in 2016, and the M.S. degree in optical engineering from the Beihang University, Beijing, China, in 2019. She is currently working toward the Ph.D. degree in mechanical engineering with the National Engineering Research Center for Electric Vehicles, Beijing Institute of Technology, Beijing, China.

Her main research interests include wireless power transfer and electric motor drive for electric vehicles.

Junjun Deng (Member, IEEE) received the B.S., M.S., and Ph.D. degrees in electrical engineering from the Northwestern Polytechnical University, Xi'an, China, in 2008, 2011, and 2015, respectively.

From 2011 to 2014, he was a Visiting Scholar with the Department of Electrical and Computer Engineer, University of Michigan, Dearborn, MI, USA. In 2016, he has joined the Faculty of Vehicle Engineering, Beijing Institute of Technology, Beijing, China. His research interests include wireless power transfer, resonant power conversion, and high performance battery chargers for electric vehicles.

Zhenpo Wang (Senior Member, IEEE) received the B.Eng. degree in mechanical design and manufacturing from the Tongji University, Shanghai, China, in 2000, and the Ph.D. degree in automotive engineering from the Beijing Institute of Technology, Beijing, China, in 2005.

He is currently a Professor with Beijing Institute of Technology, and the Director of the National Engineering Research Center for Electric Vehicles. He has authored or coauthored 4 monographs and translated books as well as more than 80 technical papers. He also holds more than 60 patents. His current research interests include pure electric vehicle integration, packaging and energy management of battery system, and charging station design.

Dr. Wang was the recipient of numerous awards including the second National Prize for Progress in Science and Technology and the first Prize for Progress in Science and Technology from the Ministry of Education, China, and the second Prize for Progress in Science and Technology from Beijing Municipal, China.

Deliang Chen received the B.S. and M.S. degrees in electrical engineering, in 2016 and 2019, respectively, from Beijing Institute of Technology, Beijing, China, where he is currently working towards the Ph.D. degree in mechanical engineering.

His research interests include high-performance circuit topology, modulation method, and control strategy, for dc power conversion, and wireless power transfer.